NANO LETTERS

Letter

pubs.acs.org/NanoLett

Measuring the Edge Recombination Velocity of Monolayer Semiconductors

Peida Zhao,[†,§] Matin Amani,[†,§] Der-Hsien Lien,[†,§] Geun Ho Ahn,[†,§] Daisuke Kiriya,[†,§] James P. Mastandrea,[‡,§] Joel W. Ager III,[‡,§] Eli Yablonovitch,[†,§] Daryl C. Chrzan,[‡,§] and Ali Javey*[,†,§]

[†]Electrical Engineering and Computer Sciences, [‡]Materials Science and Engineering, University of California at Berkeley, Berkeley, California 94720, United States

[§]Materials Sciences Division, Lawrence Berkeley National Laboratory, Berkeley, California 94720, United States

Supporting Information

ABSTRACT: Understanding edge effects and quantifying their impact on the carrier properties of two-dimensional (2D) semiconductors is an essential step toward utilizing this material for high performance electronic and optoelectronic devices. WS_2 monolayers patterned into disks of varying diameters are used to experimentally explore the influence of edges on the material's optical properties. Carrier lifetime measurements show a decrease in the effective lifetime, $\tau_{effective}$, as a function of decreasing diameter, suggesting that the edges are active sites for carrier recombination. Accordingly, we introduce a metric called edge recombination velocity (ERV) to characterize the impact of 2D material edges on nonradiative carrier recombination. The unpassivated WS_2 monolayer disks yield an ERV $\sim 4 \times 10^4$ cm/s. This work quantifies the nonradiative recombination edge effects in monolayer semiconductors, while simultaneously establishing a practical characterization approach that can be used to experimentally explore edge passivation methods for 2D materials.

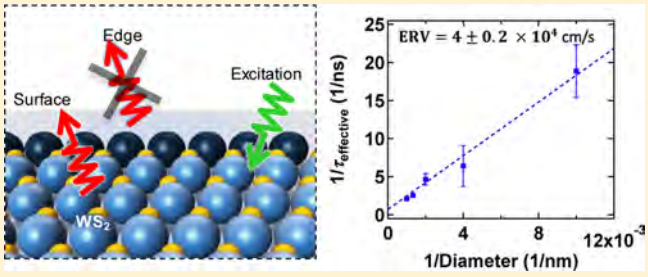

KEYWORDS: *Transition metal dichalcogenide, WS_2, edge recombination velocity, quantum yield, edge effects*

Two-dimensional (2D) semiconductors exhibit unique physical and chemical properties that make them attractive for various electronic and optoelectronic applications.[1−7] Due to their layered structure, 2D material surfaces are inherently self-terminated with well-defined chemical bonds. As a result, their unpassivated surface defect density is dramatically lower than that of most conventional 3D semiconductors. This unique surface property has enabled the observation of near-unity photoluminescence (PL) internal quantum yield (iQY) in large-area monolayer WS_2 and MoS_2 treated with superacids, demonstrating the lack of defect-mediated nonradiative surface recombination.[8−10] However, for most practical device applications, semiconductors need to be etched into proper patterns, often with small areal footprints. While the top and bottom surfaces of 2D semiconductors are chemically self-terminated, their edges can include a high density of dangling bonds that can lead to detrimental effects on carrier properties, especially when the material is patterned into small structures. In this regard, edge effects are important to be quantified and eventually controlled through proper etching and passivation.

Here, we introduce a metric called the edge recombination velocity (ERV) for 2D materials, to quantify the impact of edges on carrier recombination processes. ERV is defined as the total recombination events per unit time at the edge, divided by the product of perimeter length and excess carrier number per unit area. ERV is a direct measure of the tendency for an edge to enhance the recombination rate. Presumably, ERV depends on the detailed structure of the edge in question and can, accordingly, be altered through chemical treatments akin to those used in surface passivation. We note that ERV in a 2D material is analogous to the surface recombination velocity (SRV) used to quantify the surface quality of 3D materials.[11] ERV can be extracted by characterizing the photoluminescence properties of patterned arrays of monolayer disks. We use tungsten disulfide (WS_2) monolayers as a model material system, measuring an ERV of $\sim 4.4 \times 10^4$ cm/s after a chlorine plasma patterning.[12] The ERV value provides a baseline for 2D material edge quality and an assessment platform relevant to any optically active members of the 2D material family.

Figure 1a illustrates the expected light emitting behavior of the WS_2 monolayer disks under optical excitation, where the edge states can induce nonradiative recombination. This edge quenching is associated with the introduction of nonradiative recombination sites during the etching process and the intrinsic metallic nature of certain edge configurations.[13] To quantitatively characterize the radiative quenching, arrays of WS_2 monolayer disks of fixed diameters (d) are fabricated by lithography and dry etching. Subsequently, their PL iQY and

Received: April 27, 2017
Revised: August 10, 2017
Published: August 17, 2017

DOI: 10.1021/acs.nanolett.7b01770
Nano Lett. 2017, 17, 5356−5360

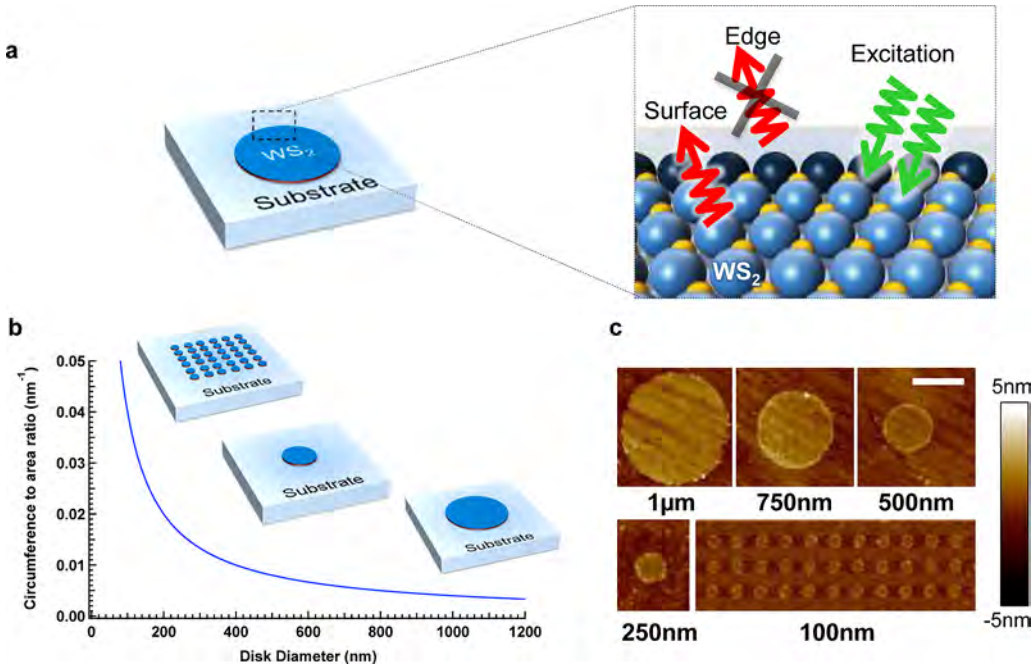

Figure 1. Experimental approach used to probe the WS_2 monolayer edge after a top-down fabrication scheme. (a) Schematic showing optical excitation response. The monolayer only emits at the surface region away from the edge, while the edge itself is expected to recombine the generated carriers nonradiatively. Note that the darker ring at the edge is illustrative only and does not accurately represent the actual atomic structure of the WS_2 edge. (b) Circumference to area ratio of disks fabricated with different diameters, showing a steady increase as diameter decreases (c) Atomic force microscopy (AFM) of WS_2 disks of all chosen diameters. Both the single disks (1 μm to 250 nm) and the array structure (100 nm) are presented. The scale bar is 500 nm for all AFM scans.

effective carrier lifetimes ($\tau_{effective}$) are measured via steady-state and time-resolved PL spectroscopy (TRPL) respectively (see SI for experimental method details).[8] The process is then repeated for different values of d. The circumference to surface area ratio increases as d decreases (Figure 1b). As a result, PL iQY and $\tau_{effective}$ are expected to decrease with decreasing d. Finally, an expression from a diffusion based model (details in the SI) can be used to predict the $\tau_{effective}$ versus d relation. A fit of the experimental data to the theoretical predictions determines the ERV. Figure 1c shows the atomic force microscopy (AFM) images of patterned WS_2 monolayer disks of varying diameters: 1 μm, 750 nm, 500 nm, 250 nm, and 100 nm. Note that, for d = 100 nm, a disk array is adapted to achieve a higher signal-to-noise ratio for photoluminescence measurements.

Figure 2a shows the PL spectra of WS_2 disks ranging from 1 μm to 100 nm in diameter, with the corresponding normalized spectra shown in the inset. The PL spectra are normalized with respect to the fill factor, directly correlating the decreasing intensity trend to an increasingly dominant edge recombination mechanism. Additionally, no obvious subgap emission or peak change is observed across spectra of different diameters shown by the inset, signifying that the radiative recombination mechanism and the optical bandgap remains unaffected for the explored diameter range.[14]

The photoluminescence internal quantum yield (PL iQY) of the WS_2 disks is extracted as a function of pump intensity (corresponding to a calculated exciton generation rate). As shown in Figure 2b, there is a monotonic decrease of iQY as d decreases. The general iQY behavior for larger d disks is consistent with the analytical model proposed in previous studies where a pump-independent and pump-dependent behavior is observed at different generation regimes.[8,10] Specifically, the generated carriers in WS_2 monolayers at steady state, G, can be balanced using a steady state recombination rate, R, via:

$$G = R = B_{nr}n^2 + B_r n^2 \tag{1}$$

where B_{nr} is the nonradiative free carrier recombination rate due to surface defects, n is the free carrier concentration, and B_r is the formation rate of excitons in the system. At the steady state, B_r can be further described via

$$B_r n^2 = \frac{\langle N \rangle}{\tau_{rad}} + C_{bx}\langle N \rangle^2 \tag{2}$$

where $\langle N \rangle$ is the exciton concentration, τ_{rad} is the radiative recombination lifetime, and C_{bx} is the biexcitonic recombination rate.

The above model includes three recombination mechanisms with distinct recombination rates (surface radiative $1/\tau_{rad}$, surface nonradiative B_{nr}, and biexcitonic C_{bx}). The first two mechanisms have the same power dependence and compete directly at the lower generation regime as $R \propto n^2 \propto \langle N \rangle$, while the last mechanism becomes dominant at higher generation regime with $R \propto \langle N \rangle^2$ and contributes to the iQY pump dependence. The model also accurately describes the experimental iQY behavior of an unetched WS_2 monolayer shown in Figure 2b and can be fitted closely utilizing similar values of $1/\tau_{rad}$ and C_{bx} mentioned in our previous work.[10] As d decreases, however, we observe a corresponding iQY decrease at lower generation regime and a convergence of iQY independent of d at the higher generation regime. The clear d dependence at lower pump power points to an edge recombination rate competing with the radiative and surface nonradiative recombination rates. The iQY convergence at higher pump power points to the previously mentioned

DOI: 10.1021/acs.nanolett.7b01770
Nano Lett. 2017, 17, 5356−5360

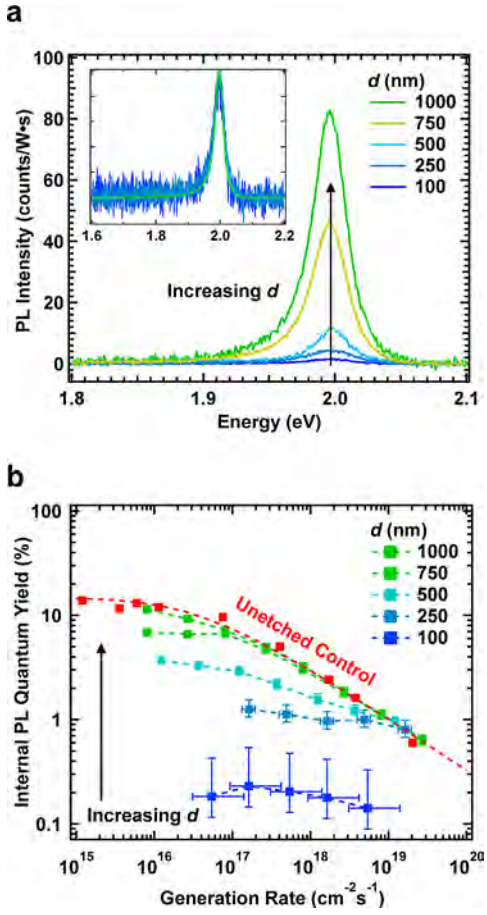

Figure 2. Optical characterizations of WS_2 monolayer disks. (a) Photoluminescence (PL) measurements of WS_2 disks with increasing diameter (corrected for fill factor), showing a steady increase in the emission intensity. The inset shows normalized spectra and indicates that no significant subgap emission is observed across all changing diameters. (b) PL internal quantum yield of WS_2 versus generation rate, as a function of disk diameter. Error bars associated with the samples originate from absorption measurements.

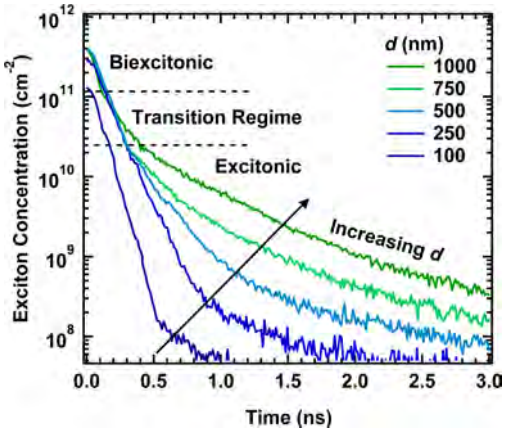

Figure 3. Time-resolved photoluminescence (TRPL) measurements of WS_2 disks. Two distinct decay regimes (with a visible transition) is observed for larger WS_2 disk sizes, while only one regime is seen for smaller sizes. The lifetime extraction is done at the lowest possible generated exciton density where monoexcitonic recombination mechanisms dominate and a clear size dependence is present.

biexcitonic recombination mechanism, overriding the d dependence. As expected, iQY at smaller d seems to exhibit minimal pump dependence, even at the higher generation rates, and is likely due to an increasingly dominant edge recombination competing with the biexcitonic recombination mechanism.

To further understand the edge recombination mechanism and measure ERV, we use TRPL to extract the lifetimes of carriers in WS_2 disks as a function of their diameters. Figure 3 shows the generated exciton concentration decay versus time of different diameter disks, demonstrating a faster lifetime decay as d decreases. As expected, two different regimes of lifetime decay are observed in the TRPL data. At the higher generated exciton density regime, biexcitonic recombination is observed (corresponding to the converging iQY in Figure 2b at the higher generation rate), dominating the lifetime decay across all disk sizes independent of d. As the exciton concentration decays over time, however, lower order recombination mechanisms become observable. These mechanisms can be classified into three types: radiative and nonradiative surface mechanisms, and a nonradiative edge mechanism. To determine the ERV, we fit a decay lifetime $\tau_{effective}$ incorporating all three aforementioned lifetime components at the lower generated exciton density assuming negligible biexcitonic recombinations. In this approximation, a single exponential decay fit can be applied via:[15]

$$\frac{d\langle N\rangle}{dt} = -\frac{\langle N\rangle}{\tau_{effective}} \quad (3)$$

where $\tau_{effective}$ conforms to the following Matthiessen's relation:

$$\frac{1}{\tau_{effective}} = \frac{1}{\tau_{rad}} + \frac{1}{\tau_{nrad}} + \frac{1}{\tau_{edge}} \quad (4)$$

Specifically, τ_{rad} and τ_{nrad} are the surface radiative and nonradiative recombination lifetime measured as 3.4 and 2.4 ns, respectively, in our previous work.[10] Decay curves in Figure 3 are fitted using both a single exponential decay at low generated exciton density as well as convoluting the single exponential decay with a measured instrument response function iteratively against experimental data to ensure accuracy.[16]

Figure 4a plots $1/\tau_{effective}$ vs $1/d$ across multiple disk samples using the previously fitted $\tau_{effective}$ values. The error bars indicate the standard deviation of all measured samples with the same designed d. To find the ERV, we first experimentally determine τ_{rad} and τ_{nrad} from an unetched WS_2 monolayer and collect them under a single time constant $\tau_{surface}$:

$$\tau_{surface} = \left(\frac{1}{\tau_{rad}} + \frac{1}{\tau_{nrad}}\right)^{(-1)} = 1.37 \text{ ns} \quad (5)$$

Subsequently, τ_{edge} is extracted from the measured $\tau_{effective}$ for each disk diameter. Using the diffusion model presented in Supporting Information, τ_{edge} and ERV are related by the following expression:

$$\tau_{edge} = \frac{d}{4 \times \text{ERV}} \quad (6)$$

where ERV has units of length/time.

With eq 6, we fit the experimental $1/\tau_{effective}$ vs $1/d$ curve with a linear slope of (4× ERV) and find an ERV of $\sim 4 \pm 0.2 \times 10^4$ cm/s. Notably, the y-intercept of the fitted line also directly indicates the asymptotic value of $\tau_{effective}$ where $\tau_{effective}$ approaches $\tau_{surface}$ as d approaches infinity.

DOI: 10.1021/acs.nanolett.7b01770
Nano Lett. 2017, 17, 5356−5360

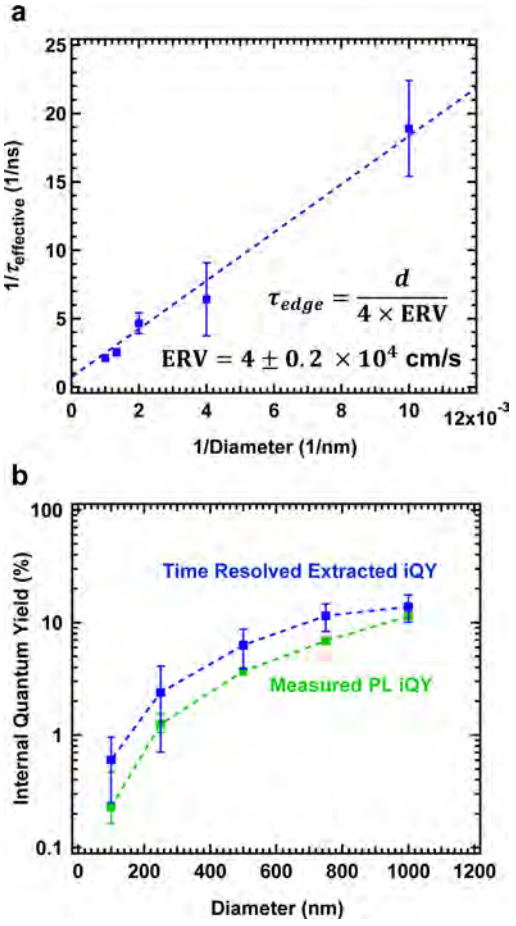

Figure 4. (a) Reciprocal of effective lifetime measured by TRPL versus reciprocal of diameter. Error bars signify the standard deviation of multiple samples of the same designed diameter. (b) Extracted internal quantum yield from both steady-state PL (green) and TRPL (blue) measurements. Error bars on the steady-state PL iQY curve represent absorption error.

It is important to compare the steady-state PL iQY in Figure 2b against the lifetime measurements shown in Figure 3 to verify self-consistency between the two experiments. To this end, we directly compare the iQY values extracted from both measurements. For the TRPL data in Figure 3, we find the time-resolved extracted iQY via:

$$\text{iQY} = \frac{\tau_{\text{effective}}}{\tau_{\text{rad}}} \tag{7}$$

Figure 4b shows from the iQY comparison between quantities calculated from measured decay curves of TRPL (blue) and those directly extracted from steady state PL (green) at the low excitation regime. Both sets of iQY values show a similar trend of decay and are in good agreement. The error bars on the PL iQY curve represent the uncertainty in the absorption measurements, while the error bars on time-resolved extracted iQY curve reflect the spread in the extracted $\tau_{\text{effective}}$ mentioned previously.

To understand ERV as a metric of nonradiative edge recombination in 2D semiconductors, we draw attention to a similar metric extensively utilized by the optoelectronics community, called surface recombination velocity (SRV). SRV is used for describing the surface quality of a 3D semiconductor by quantifying the nonradiative carrier recombination sites at the surface and is a key figure of merit for projecting the maximum performance of the enabled optoelectronic devices based on a 3D semiconductor.[11] Generally, SRV can range from high quality passivated silicon surface of <1 cm/s to unpassivated silicon surfaces spamming into the 10^4–10^5 cm/s regimes.[17−19]

Similar to SRV and the critical role it plays in quantifying surface recombination, ERV can also serve as a key figure of merit for nonradiative carrier recombination at the edge of 2D materials. To see this, we define ERV as

$$\text{ERV} = (N_t/l)\sigma_{1D}\upsilon_{\text{th}} \tag{8}$$

where N_t/l is a linear density of nonradiative recombination sites along a defined perimeter, σ_{1D} is the atomic capture radius of diffusing excitons, and υ_{th} is the thermal velocity of excitons. Equation 8 follows from the general lifetime expression:

$$\frac{1}{\tau_{\text{edge}}} = \frac{N_t}{A}\sigma_{1D}\upsilon_{\text{th}} \tag{9}$$

and making the appropriate substitution from eq 6 where N_t/A is the areal density of nonradiative recombination sites.

Equation 8 allows us to calculate the density of nonradiative recombination sites at a 2D material edge. To illustrate this, we approximate the nonradiative edge recombination sites density N_t/l on our measured WS_2 system using a capture radius on the order of the atomic radius $\sigma_{1D} \sim 10^{-8}$ cm and an exciton thermal velocity $\upsilon_{\text{th}} \sim 10^5$ cm/s.[20,21] The υ_{th} value is estimated using experimentally measured diffusion length of excitons in transition metal dichalcogenides (10^{-4}–10^{-5} cm) divided by the measured lifetime (~1·ns).[22,23] The value used also falls within the range of reported exciton υ_{th} from inorganic materials such as GaAs/AlGaAs quantum wells and thin silicon (10^6 to 10^7 cm/s) to organic molecules such as anthracene (10^4 cm/s).[24−27] With our measured ERV, we calculate $N_t/l \approx 4.4 \times 10^7$ cm^{-1}, corresponding to a nonradiative recombination site per ~2 Å edge length. The estimated density hints at nonradiative recombination at nearly every edge atom, underlying the need for better passivation schemes in the future. This is expected given that certain edge orientations are calculated to exhibit metallic behavior.[13]

In summary, a simple direct optical characterization method enables the experimental measurement of ERV, a quantitative metric directly related to the optical quality of the edge of 2D materials. Using WS_2 as a model material system, we measure ERV of 4×10^4 cm/s for Cl-plasma etched edges. The approach can be extended to other optically active 2D semiconductors. In the future, ERV can be used as an edge quality metric to explore the effectiveness of different edge passivation schemes.

■ ASSOCIATED CONTENT

Supporting Information

The Supporting Information is available free of charge on the ACS Publications website at DOI: 10.1021/acs.nanolett.7b01770.

Optical measurement details, laser spot size calibration, absorption measurements, additional lifetime data, PMMA A2 effects, chlorine plasma etching results, detailed fabrication methods, and τ_{edge} derivation via the diffusion equation (PDF)

DOI: 10.1021/acs.nanolett.7b01770
Nano Lett. 2017, 17, 5356−5360

AUTHOR INFORMATION

Corresponding Author

*E-mail: ajavey@eecs.berkeley.edu.

ORCID

Der-Hsien Lien: 0000-0001-6774-2074
Joel W. Ager III: 0000-0001-9334-9751
Ali Javey: 0000-0001-7214-7931

Notes

The authors declare no competing financial interest.

ACKNOWLEDGMENTS

Nanofabrication and processing of monolayers were supported by NSF E3S Center. PL, TRPL, and absorption measurements were supported by the Electronic Materials Program, funded by Director, Office of Science, Office of Basic Energy Sciences, Materials Sciences and Engineering Division of the U.S. Department of Energy under contract no. DE-AC02-05Ch11231.

ABBREVIATIONS

2D, two dimension
iQY, internal quantum yield
PMMA, poly(methyl methacrylate)
PL, photoluminescence
PL iQY, photoluminescence internal quantum yield
TRPL, time-resolved photoluminescence
SRV, surface recombination velocity
ERV, edge recombination velocity

REFERENCES

(1) Fang, H.; Chuang, S.; Chang, T. C.; Takei, K.; Takahashi, T.; Javey, A. *Nano Lett.* **2012**, *12* (7), 3788−3792.
(2) Li, D.; Cheng, R.; Zhou, H.; Wang, C.; Yin, A.; Chen, Y.; Weiss, N. O.; Huang, Y.; Duan, X. *Nat. Commun.* **2015**, *6*, 7509.
(3) Radisavljevic, B.; Radenovic, A.; Brivio, J.; Giacometti, V.; Kis, A. *Nat. Nanotechnol.* **2011**, *6* (3), 147−150.
(4) Ross, J. S.; Klement, P.; Jones, A. M.; Ghimire, N. J.; Yan, J.; Mandrus, D. G.; Taniguchi, T.; Watanabe, K.; Kitamura, K.; Yao, W.; Cobden, D. H.; Xu, X. *Nat. Nanotechnol.* **2014**, *9* (4), 268−272.
(5) Sundaram, R. S.; Engel, M.; Lombardo, A.; Krupke, R.; Ferrari, A. C.; Avouris, P.; Steiner, M. *Nano Lett.* **2013**, *13* (4), 1416−1421.
(6) Tosun, M.; Chuang, S.; Fang, H.; Sachid, A. B.; Hettick, M.; Lin, Y.; Zeng, Y.; Javey, A. *ACS Nano* **2014**, *8* (5), 4948−4953.
(7) Desai, S. B.; Madhvapathy, S. R.; Sachid, A. B.; Llinas, J. P.; Wang, Q.; Ahn, G. H.; Pitner, G.; Kim, M. J.; Bokor, J.; Hu, C.; Wong, H.-S. P.; Javey, A. *Science* **2016**, *354* (6308), 99−102.
(8) Amani, M.; Lien, D.-H.; Kiriya, D.; Xiao, J.; Azcatl, A.; Noh, J.; Madhvapathy, S. R.; Addou, R.; Kc, S.; Dubey, M.; Cho, K.; Wallace, R. M.; Lee, S.-C.; He, J.-H.; Ager, J. W.; Zhang, X.; Yablonovitch, E.; Javey, A. *Science* **2015**, *350* (6264), 1065.
(9) Amani, M.; Burke, R. A.; Ji, X.; Zhao, P.; Lien, D.-H.; Taheri, P.; Ahn, G. H.; Kirya, D.; Ager, J. W.; Yablonovitch, E.; Kong, J.; Dubey, M.; Javey, A. *ACS Nano* **2016**, *10* (7), 6535−6541.
(10) Amani, M.; Taheri, P.; Addou, R.; Ahn, G. H.; Kiriya, D.; Lien, D.-H.; Ager, J. W.; Wallace, R. M.; Javey, A. *Nano Lett.* **2016**, *16* (4), 2786−2791.
(11) Shockley, W. *Electrons and Holes in Semiconductors with Applications to Transistor Electronics*; D. Van Nostrand Company, Inc: Princeton: New York, 1950; p 576.
(12) Lin, T.; Kang, B.; Jeon, M.; Huffman, C.; Jeon, J.; Lee, S.; Han, W.; Lee, J.; Lee, S.; Yeom, G.; Kim, K. *ACS Appl. Mater. Interfaces* **2015**, *7* (29), 15892−15897.
(13) Huo, N.; Li, Y.; Kang, J.; Li, R.; Xia, Q.; Li, J. *Appl. Phys. Lett.* **2014**, *104* (20), 202406.
(14) Tongay, S.; Suh, J.; Ataca, C.; Fan, W.; Luce, A.; Kang, J. S.; Liu, J.; Ko, C.; Raghunathanan, R.; Zhou, J.; Ogletree, F.; Li, J.; Grossman, J. C.; Wu, J. *Sci. Rep.* **2013**, *3*, 2657.
(15) Ivan Pelant, J. V. *Luminescence Spectroscopy of Semiconductors*; Oxford University Press: New York, 2012; p 542.
(16) Preus, S. *DecayFit - Fluorescence Decay Analysis Software*, 1.4; FluorTools, 2014.
(17) Wolford, D. J.; Gilliland, G. D.; Kuech, T. F.; Smith, L. M.; Martinsen, J.; Bradley, J. A.; Tsang, C. F.; Venkatasubramanian, R.; Ghandi, S. K.; Hjalmarson, H. P. *J. Vac. Sci. Technol., B: Microelectron. Process. Phenom.* **1991**, *9* (4), 2369−2376.
(18) Baek, D.; Rouvimov, S.; Kim, B.; Jo, T.-C.; Schroder, D. K. *Appl. Phys. Lett.* **2005**, *86* (11), 112110.
(19) Yablonovitch, E.; Allara, D. L.; Chang, C. C.; Gmitter, T.; Bright, T. B. *Phys. Rev. Lett.* **1986**, *57* (2), 249−252.
(20) Nakamura, M.; Suzuki, T.; Fujita, M. *Phys. Rev. B: Condens. Matter Mater. Phys.* **1987**, *35* (6), 2854−2862.
(21) Schramm, G. *Phys. Status Solidi A* **1991**, *125* (2), K113−K116.
(22) Kato, T.; Kaneko, T. *ACS Nano* **2016**, *10* (10), 9687−9694.
(23) Kumar, N.; He, J.; He, D.; Wang, Y.; Zhao, H. *J. Appl. Phys.* **2013**, *113* (13), 133702.
(24) Harris, C. I.; Monemar, B.; Holtz, Ro.; Kalt, H.; Mert, J. L. *J. Phys. IV* **1993**, *03* (C5), 171−174.
(25) Tamor, M. A.; Wolfe, J. P. *Phys. Rev. Lett.* **1980**, *44* (25), 1703−1706.
(26) Avakian, P.; Merrifield, R. E. *Mol. Cryst.* **1968**, *5* (1), 37−77.
(27) Levinson, J.; Weisz, S. Z.; Cobas, A.; Rolón, A. *J. Chem. Phys.* **1970**, *52* (5), 2794−2795.

DOI: 10.1021/acs.nanolett.7b01770
Nano Lett. 2017, 17, 5356−5360